



Published in final edited form as:

ACS Nano. 2009 June 23; 3(6): 1379–1388. doi:10.1021/nn900118a.

Magnetic-Plasmonic Core-Shell Nanoparticles

Carly S. Levin[†], Cristina Hofmann[†], Tamer A. Ali[§], Anna T. Kelly[†], Emilia Morosan[§], Peter Nordlander^{§,§}, Kenton H. Whitmire[†], and Naomi J. Halas^{†,§,*}

[†] Department of Chemistry, Rice University, P.O. Box 1892, Houston, Texas, 77251-1892.

[§] Department of Physics and Astronomy, Rice University, P.O. Box 1892, Houston, Texas, 77251-1892.

[§] Department of Electrical and Computer Engineering, Rice University, P.O. Box 1892, Houston, Texas, 77251-1892.

Abstract

Nanoparticles composed of magnetic cores with continuous Au shell layers simultaneously possess both magnetic and plasmonic properties. Faceted and tetracubic nanocrystals consisting of wüstite with magnetite-rich corners and edges retain magnetic properties when coated with an Au shell layer, with the composite nanostructures showing ferrimagnetic behavior. The plasmonic properties are profoundly influenced by the high dielectric constant of the mixed-iron-oxide nanocrystalline core. A comprehensive theoretical analysis that examines the geometric plasmon tunability over a range of core permittivities enables us to identify the dielectric properties of the mixed-oxide magnetic core directly from the plasmonic behavior of the core-shell nanoparticle.

Keywords

wüstite nanocrystals; core-shell nanostructure; surface plasmon resonance; bifunctional; magnetic nanoshells

Currently there is great interest in the development of nanoparticles that combine multiple functions or properties not obtainable in individual materials.^{1, 2} New nanoparticles that combine an optical signature with other physical properties are particularly useful, enabling optical addressability for tracking or monitoring particles in addition to other properties. A very useful strategy for imparting optical properties at the nanoscale involves the integration of noble metals, and their associated localized surface plasmons, into the particle or structure. The growth of a thin Au shell layer around a functional nanoparticle core provides a practical and highly general approach for adding optical addressability to virtually any type of nanoparticle.^{3, 4} Au shell layers provide a strong plasmon resonant optical response to the nanoparticle, with a resonant frequency determined by geometry, the dielectric

* Corresponding Author: halas@rice.edu.

Supporting Information Available: Additional information includes a comparison of the electric field enhancement distribution for nanoshells with three different core shapes, a Raman spectrum of the iron oxide nanoparticles, magnetization measurements as a function of temperature, a histogram of the particles used for SQUID measurements, and XPS spectra of the iron oxide nanoparticles. This material is available free of charge via the Internet at <http://pubs.acs.org>.

properties of the nanoparticle core and the surrounding medium of the nanoparticle.⁵ In addition, the Au shell layer provides a relatively chemically inert surface layer that can be functionalized to enhance solubility in various media, promote biocompatibility, and preserve the properties of the core material.

In this paper we report the combination of resonant optical and magnetic properties in a single nanostructure, accomplished by the growth of an Au shell layer around magnetic iron oxide nanoparticle cores. Previously reported studies combining plasmonic and magnetic nanostructures have focused largely on iron,⁶⁻⁹ the thermodynamically favorable forms of iron oxides such as magnetite,¹⁰⁻¹² and silica-magnetite composites.^{10, 13, 14} Generally, partial coverage of small gold nanoparticles bound to the surface of the iron oxide particles has been achieved, but attaining uniform, continuous Au layers has been a challenge.¹⁵ Here we show that wüstite (Fe_xO) nanocrystals,¹⁶⁻²² which can also form oxides of higher oxidation states, can be used as a magnetic core material and initial precursor for continuous gold shell layer growth. Wüstite nanocrystals can be grown in a variety of shapes and sizes; however, the subsequent addition of an Au layer on the nanocrystal surface modifies the overall nanoparticle shape, resulting in a spherical or near-spherical morphology with a nonspherical core. In addition to a complex morphology, the dielectric properties of nanocrystalline wüstite can also be complex, dependent upon other Fe oxides that may be present in the edges or corners of the nanocrystal. Optical measurements combined with theoretical analysis of the plasmon-resonant response of the wüstite core-Au shell nanostructures allow us to deduce the permittivity of the wüstite-mixed-oxide core nanocrystals. While plasmonic nanoparticles have been used extensively as localized surface plasmon resonant nanosensors of their environment, this is the first case of the use of plasmonic properties to assess the dielectric properties of an embedded nanomaterial within the nanoparticle itself.

The use of wüstite precursors as a magnetic core material offers several unique advantages in the design of multifunctional magnetic nanoparticles. The metastability of wüstite provides control over the size and shape of the nanocrystal, whose properties can also be varied with composition, by the generation of mixed phases of wüstite, magnetite, and iron in the nanocrystalline structure. This can be accomplished by annealing in inert or oxidizing atmospheres, or by heating the nanocrystals in a high boiling point solvent, such as hexadecane.²³ Through manipulation of the material composition in these ways, the magnetic behavior could be tailored to a specific application or device. Wüstite may provide a preferable core material for mixed magnetic-plasmonic nanoparticles since traditional magnetic nanomaterials aggregate even after Au coating due to an extremely strong magnetic attraction.²⁴ Further, since the material itself can undergo oxidation, utilization of this core material offers an advantage in control over the percentage of magnetic material per particle as compared to composite structures where subsequent steps may be used to attach magnetic material to a nonmagnetic core particle.¹³

RESULTS AND DISCUSSION

Au shell layer growth on wüstite nanocrystals is a relatively straightforward synthetic procedure.²⁵⁻²⁷ Various stages of the growth process are depicted in schematic form (Fig. 1

A, D). The nanoparticle morphologies at various stages of the growth process are imaged using transmission electron microscopy (Fig. 1 B,C and E,F). To grow the Au shell layer on the nanocrystals, we began with monodisperse wüstite nanocrystals of either faceted (Fig. 1 B,C i) or tetracubic (Fig. 1 E,F i) shape, with approximate radii of 31.5 ± 9.7 nm and 28.5 ± 7.3 nm, respectively. The synthesized particles were surfactant stabilized, which presents a noticeable thin, almost transparent layer around the particles in the TEM images in Figure 1. The nanocrystals were then functionalized with an amine-terminated linker molecule which displaces the surfactant and allows for the attachment of ~ 2 nm Au colloid to the nanocrystal surface (Fig. 1 B,C and E,F ii). The immobilized colloidal gold acts as nucleation sites for electroless gold plating onto the precursor nanoparticles to form a continuous gold shell (Fig. 1 B,C and E,F iii, shown here with an approximate 27 nm shell thickness). The thickness of the gold shell layer can be controlled by varying the concentration of AuCl_4^- in the final reduction step. Although the nanocrystalline cores are faceted or tetracubic in shape, the Au shell layer growth results in spherically shaped particles.

The core-shell geometry of the fabricated nanoparticles supports a plasmon resonant response dependent upon nanocrystalline core size, Au shell layer thickness, and the dielectric properties of the core, shell, and embedding medium.⁵ Silica core-Au shell nanoshells²⁸ demonstrate strong resonance absorption in the visible and near-infrared (NIR). For the silica-Au nanoshell structure, the plasmon absorption band shifts to shorter wavelengths as the thickness of the gold shell is increased. In contrast, it has been observed that magnetite iron oxide cores with Au shell layers show a redshifted plasmon absorption peak with increasing shell thickness.²⁹

Extinction spectra of the wüstite core-Au shell nanoparticles in solution are shown in Figure 2 A,B. The large core size of the nanoparticles (average approximate radii 32 and 29 nm, respectively) and the thick Au shell layers (from 11 to 45 nm) allow for a prominent surface plasmon resonance peak. As the shell thickness increases (Fig. 2 A,B iii-vi), the plasmon peaks shift to longer wavelengths. An optical image (Fig. 2C) of the particles represented in Figure 2A shows the corresponding change in color of the nanoparticles suspended in aqueous solution with increasing shell layer thickness. The wide range of colors displayed resulting from the variation in Au shell layer thickness allows for the potential use of these nanoparticles for spectroscopic or colorimetric labeling.^{30, 31}

The anomalous plasmon redshift with increasing Au shell layer thickness observed for iron oxide cores can be understood in terms of plasmon hybridization.^{32, 33} In this picture, the sphere plasmons associated with the outer surface of the shell layer interact with the cavity plasmons associated with the inner surface of the shell (Fig. 3). Two hybridized plasmons result from this interaction, a “bright” or “bonding” plasmon that couples strongly to the incoming and outgoing light waves and a “dark” or “antibonding” nanoshell plasmon mode that couples poorly to the electromagnetic far field. The coupling of a plasmon mode to incident electromagnetic radiation is proportional to the square of the dipole moment of the plasmon mode. A bright plasmon mode is a plasmon mode with a large dipole moment and a dark plasmon mode is a plasmon mode with a small dipole moment. For the case of a nanoshell composed of a core nanoparticle with a low dielectric permittivity such as vacuum or silica, the cavity plasmon is at a higher energy than the sphere plasmon. In this case the

low energy hybridized plasmon is a bright plasmon, being more “spherelike”, and the high energy hybridized plasmon is a dark plasmon, being more “cavitylike”. In this low permittivity regime, the extinction spectrum is dominated entirely by the low energy bonding nanoshell plasmon. For increasing shell thickness, the interaction between the cavity and sphere modes decreases, resulting in a blueshift of the bonding mode and a redshift of the antibonding mode (Fig. 3A). For the case of a high permittivity core material such as iron oxide, the cavity plasmon is redshifted to an energy below that of the sphere plasmon (Fig. 3B). In this regime the higher energy antibonding nanoshell plasmon will have the largest excitation cross-section, since it consists primarily of the dipole-active sphere plasmon. However, the lower energy bonding plasmon with its dominant contribution of the cavity plasmon will also be present in the spectrum. The primitive cavity plasmon acquires a dipole moment in the presence of the core. For increasing shell thickness, the high energy bright antibonding plasmon will redshift and the low energy bonding plasmon will blueshift. The experimentally observed spectral redshift with increasing shell layer thickness is, therefore, consistent with the case of a nanoshell with a large permittivity core material, and agrees with the plasmonic properties of other iron oxide core-Au shell nanoparticles that have been reported.^{27, 29}

To better understand the plasmonic properties of our wüstite-core Au-shell nanoparticles, we investigated the effects of the various core shapes fabricated on the plasmonic properties of spherical core-shell nanoparticles using the Finite-Difference Time-Domain (FDTD) method. A realistic gold dielectric function was used in these calculations.^{34, 35} A comparison of the extinction spectra for nanoshells of spherical, cubic, and concave cubic cores which have the same core and shell volumes is shown in Figure 4A, for the case of a low permittivity core (silica), and Figure 4B, for a model high permittivity core case ($\epsilon = 12.0$). For a silica core material (Fig. 4A), the dipolar resonances for the nanoparticles with cubic and concave cubic cores are slightly redshifted compared to the nanoshell with a spherical core. For the cubic core, and more strongly for the concave cubic core, an additional quadrupolar plasmon resonance appears at nominally 540 nm. Figure 4B shows the calculated spectra for the same structures in Figure 4A, but with cores filled with an $\epsilon = 12.0$ artificial material. In this case, the bonding modes of the cubic and concave cubic cores are damped and higher order modes are excited. The experimentally observed plasmon mode is the antibonding dipolar resonance, which is the main resonance in the concave cubic core case.

The differences in the optical properties of core-shell plasmonic nanoparticles introduced by a nonspherical core are due to the reduction of symmetry introduced by the variations in core geometries. For a system of spherical symmetry, only primitive plasmons of the same multipolar symmetry interact and hybridize.^{36, 37} The spectrum for the spherical core in Figure 4A, for example, displays only dipolar nanoshell resonances due to the hybridization of the dipolar sphere plasmon mode with the dipolar cavity plasmon mode. When the spherical symmetry of the core is broken, however, primitive plasmons of different multipolar symmetry can interact, resulting in the appearance of new modes in the spectrum due to the mixing of, for example, dipolar sphere plasmon modes with higher order cavity plasmon modes. This additional interaction also leads to larger shifts of the hybridized plasmon resonances. For the cubic silica core spectrum shown in Figure 4A, the symmetry

breaking is relatively weak and results in a redshift of the dipole resonance and the appearance of a weak quadrupolar resonance discerned as a slight shoulder at 540 nm on the short wavelength side of the dipolar resonance. For the concave cubic core, this effect is stronger, resulting in a more significant redshift of the dipolar mode and the appearance of a clearly distinguishable quadrupolar plasmon resonance at 540 nm. The calculated localized surface plasmon resonance (LSPR) shifts of the bonding dipolar nanoshell resonance as a function of shell thickness for the three different silica core shapes is shown in Figures 4C,D, for low (*e.g.*, silica) and high permittivity cores, respectively. To allow for a meaningful comparison of the optical properties of nanoshells of different core shapes, an effective core radius r_{eff} , defined as the radius of a spherical core of the same volume as the actual core, is used. For the silica permittivity case, a blueshift of the bonding nanoshell resonance is clearly observed with increasing shell thickness: for the high permittivity case, the opposite trend is observed. The qualitative features of these wavelength shifts do not depend strongly on the detailed shape of the core. (Local field enhancements for the lowest order dipolar modes of the structures depicted in Figure 4 are shown in the Supporting Information Figure S1.) This analysis reveals that the shape of the dielectric core has only a minor influence on the extinction spectra and that core geometry does not affect the experimentally observed shell thickness dependent plasmon wavelength shifts.

Based on this analysis, the dielectric permittivity of the core material, not the shape of the core, is a major controlling factor in the plasmon resonant response of core-shell nanoparticles. We can take advantage of the dependence of the plasmonic properties on core permittivity to estimate the dielectric properties of the core nanomaterial. This is important, since it provides a method for measuring the dielectric permittivity of nanocrystals or nanoparticles. This method is limited to study of dielectric functions of nanomaterials around which a plasmonic shell is grown. Despite the limited accuracy of this approach, it is to our knowledge the only available method for estimating the dielectric properties of nanocrystals or nanoparticles, which may differ significantly from the dielectric properties of the bulk phases of the material. This is particularly of interest for the case of exotic nanomaterials, such as wüstite nanocrystals, where mixed oxidation states of iron oxide may be intentionally or unintentionally introduced into the nanostructure. To examine the core permittivity dependence of the plasmonic properties, the plasmon resonant response of Au nanoshells with a spherical core for a large range of core permittivities was calculated using Mie theory (Fig. 5). Core permittivities ranging from $\epsilon = 2$ to $\epsilon = 22$ were calculated for the same size core-shell nanostructures. In each case, the core radius was $r_1 = 36$ nm, and the outer radius of the nanoparticle r_2 was varied between 50 and 70 nm (Fig. 5A). From this comprehensive mapping of the plasmonic properties of the core-shell structure, we can clearly observe the thickness-dependent plasmon resonant wavelength shifts and their dependence on core permittivity. From the waterfall plots of Figure 5A, we see that for lower values of the core permittivity there is essentially no wavelength shift of the plasmon resonance for the r_1 and r_2 values studied. As the core permittivity is increased, however, several changes in the plasmonic properties are introduced. Figures 5B, C, and D show representative spectra extracted from the waterfall plots of Figure 5A for cores with $\epsilon = 2$, 12, and 22, for qualitative comparison to our experimental spectra. In these spectra we see that for core permittivities smaller than 8, the low energy bonding mode always blueshifts

and is attenuated with increasing shell thickness. For core permittivities larger than 8, the antibonding mode becomes visible, and a strong redshift of this mode with increasing shell thickness is apparent for core permittivities of 10 and above. Although the experimentally determined permittivities for bulk wüstite and magnetite are smaller than 8 in the wavelength region of interest,³⁸ simulations modeling the core using bulk permittivity values, or a combination of both, do not show qualitative agreement with our experimental observations. The best match to our experimental data is found for $\epsilon = 12$ (Fig. 5C). From these observations we conclude that the effective permittivity of our nanocrystalline cores is quite likely in the $\epsilon = 10$ -14 range, significantly larger than bulk permittivity measurements which range from $\epsilon = 4.8$ to 5.8 for wüstite and $\epsilon = 5.5$ to 6.1 for magnetite in our wavelength range.^{38, 39}

To determine the crystallinity and structure of the iron oxide core nanoparticles in the nanoshell composites, powder X-ray diffraction (XRD) was utilized. As shown in Figure 6, the peak position and relative intensity of all diffraction peaks for the three products match well with standard powder diffraction data. The wüstite peaks correlate with a cubic phase with cell parameters $a = c = 4.32 \text{ \AA}$ and space group $Fm\bar{3}m$ (225) (JCPDS card no. 98-000-0464). The presence of additional peaks in the XRD spectra (Fig. 6 A,B) shows a slight oxidation of wüstite to magnetite. The existence of magnetite in the XRD spectra of the particles is due to mild oxidation of the outermost layer of the originally formed metastable wüstite nanoparticles. After decomposition, these particles are exposed to air, which results in the formation of a thin layer of magnetite on the surface and edges of the particles. Since both magnetite and maghemite ($\gamma\text{-Fe}_2\text{O}_3$; P4₃32; no.212; $a = 8.346 \text{ \AA}$) have the same cubic inverse spinel structure and unit cells with only *ca.* 1% difference,⁴⁰ Raman spectroscopy (Supporting Information Fig. S2) was used to confirm that maghemite was not present.⁴¹ XPS data (Supporting Information Fig. S5 and Table S1) also confirms the presence of magnetite as well as a small (< 10 %) amount of elemental Fe. This is consistent with the reported decomposition of wüstite.⁴² The magnetite crystals present in the iron oxide cores have a cubic phase with cell parameters $a = c = 8.3969 \text{ \AA}$ and space group $Fd\bar{3}m$ (227) (JCPDS card no. 98-000-0294). Our group has previously published detailed characterization including dark field TEM images and selected area electron diffraction patterns for single crystals prepared under the same reaction conditions in Hofmann *et al.*²³ The reported data presents unequivocal evidence that the core of the nanoparticle is composed of wüstite and the distribution of magnetite is concentrated to the corners and edges. Interestingly, the Fe_3O_4 domains exist within the predominant Fe_xO crystal lattice of the nanoparticle and remain aligned with it. Once the iron oxide is functionalized and decorated with small Au nanoparticles for Au shell layer growth, a small peak attributed to gold can be observed (Fig. 6A ii). When a continuous Au shell is formed on the particles (with a thickness of 10.9 nm), the diffraction from Au dominates the pattern (Fig. 6A iii), due to its high electron density.⁴³ The Au diffraction peaks indicate a cubic phase of Au with cell parameters $a = c = 4.0786 \text{ \AA}$ and space group $Fm\bar{3}m$ (225) (JCPDS card no. 98-000-0230).

To test if the particles were macroscopically magnetic, a permanent magnet was placed adjacent to the vials of Au-decorated iron oxide precursors and Au-coated iron oxide

nanoparticles (Fig. 7A). The materials were attracted to the magnet, leaving the solutions transparent. A high magnification SEM image (Fig. 7B), representative of the nanoparticles shown in Figure 7A, verifies that the particles are magnetic even with a complete, continuous Au coating.

Since the various iron oxides possess different magnetic properties, magnetic measurements were performed to better characterize the magnetic properties of this mixed oxide system. Magnetite is a well-known ferrimagnetic material, while wüstite is antiferromagnetic¹⁷ or weakly ferrimagnetic^{44, 45}. In ferrimagnetic materials, the magnetic moments of the two sublattices align antiparallel, but do not cancel. This type of magnetic ordering differs from ferromagnetism and antiferromagnetism, where in the former, all of the magnetic ions align parallel to each other, and in the latter, there are two sublattices with magnetic moments exactly equal but which align antiparallel, and the net moment is zero in zero magnetic field. Alignments of these sublattices occur below a certain critical temperature, called the Curie temperature T_C (for ferromagnets and ferrimagnets) or the Néel temperature T_N (for antiferromagnets).

Magnetite has a Curie temperature (T_C) of 858 K,⁴⁶ where T_C is defined as the temperature above which a ferromagnetic or ferrimagnetic material becomes paramagnetic.⁴⁷ A paramagnetic material requires an externally applied magnetic field to retain any magnetization. Wüstite has a Néel temperature (T_N) of ~ 195 K,⁴⁸ where T_N is defined as the temperature above which an antiferromagnetic material becomes paramagnetic.⁴⁹ For wüstite, this change from an antiferromagnetic or weakly ferrimagnetic material to a paramagnetic material is accompanied by a change in crystal structure from monoclinic or rhombohedral to a cubic phase.¹⁷ When an external field is applied to an antiferromagnetic material, a slow increase of the magnetization with field is to be expected; however, for a ferrimagnetic material, this change is expected to increase faster than that of an antiferromagnetic material. Therefore, any magnetic behavior of these nanoparticles below T_C is expected to be dominated by the presence of magnetite and any contribution from iron.

Field-dependent magnetization measurements $M(H)$ were performed at two temperatures, $T = 100$ K and 250 K, (Fig. 8) chosen to confirm that at different temperatures below the $T_C = 858$ K, similar results are observed. Zero field-cooled (ZFC) magnetization measurements as a function of temperature $M(T)$ (Supporting Information Fig. S3) show that at 300 K there is still an increase in magnetization. Above a temperature where the system enters the superparamagnetic state (known as the blocking temperature) a maximum should be expected in $M(T)$. The absence of such a local maximum in our $M(T)$ data (Supporting Information Fig. S3) indicates that the material has not yet entered a superparamagnetic state. The magnetization measurements $M(H)$ shown in Figure 8 indicate that there is no significant change in the coercivity of uncoated and coated iron oxide particles. The coercivity of the materials is 58.4 ± 3.2 mT at 100 K and 35.3 ± 0.5 mT at 250 K for the uncoated particles and 52.5 ± 2.4 mT at 100 K and 33.5 ± 1.0 mT at 250 K for those coated with an Au shell layer. At the maximum field for these measurements ($H = 5$ T), the magnetization still has a small positive slope, and, therefore, the saturation magnetization can be expected to be slightly higher than that at 5 T. The remanent magnetization of the iron oxide nanoparticles is 0.8374 ± 0.0148 emu/g at 100 K and 0.8659 ± 0.0152 emu/g at

250 K for the uncoated particles and 0.0387 ± 0.0199 emu/g at 100 K and 0.0360 ± 0.0196 emu/g at 250 K for the Au coated nanoparticles. Since the mass used to determine the saturation magnetization and the remanent magnetization values includes both the mass of the iron oxide core and Au shell in the Au coated samples, a decrease in the saturation magnetization and remanent magnetization results largely from the addition of a non-magnetic mass, that is, the Au layer.

While ultrasmall Au nanoparticles have demonstrated ferromagnetism,⁵⁰ at diameters larger than 4 nm, the magnetism reverts back to that of the bulk state Au,⁵¹ where Au is known to have diamagnetic properties. For thin Au films on glass and polypropylene, a diamagnetic response is characterized by a linear relationship between magnetization and applied field: $M \propto -H$.⁵² However, for these gold coated iron oxide nanoparticles, a hysteresis loop can be observed as shown in the insets of Figure 8 A,B. Therefore, the typical magnetic behavior of bulk gold is not observed in these samples, and after Au coating, the nanoparticle still exhibits ferrimagnetic behavior.

We have shown that nanoparticles consisting of a wüstite core with magnetite-rich corners and edges can be coated with a continuous gold shell in aqueous solution at room temperature. The procedure converts hydrophobic iron oxide nanoparticles to water soluble Au coated bifunctional nanoparticles and can be extended to the immobilization of other noble metals. The Au shell provides a surface for chemical functionality and long-term stabilization of the core material. Additionally, controlled oxidation of metastable wüstite by varying exposure of the particles to different environmental conditions allows for tunability over the materials' magnetic properties while varying the Au shell thickness provides tunability of the plasmonic properties. Theoretical analysis of the plasmonic properties of these nanoparticles suggests that the plasmonic redshift that occurs with increasing Au shell thickness is due to a large dielectric permittivity of the core. Based on our simulations we estimate the core nanocrystal permittivity to be in the $\epsilon = 10-14$ range, larger than the bulk permittivities of wüstite and magnetite previously reported. The exhibited ferrimagnetic properties of the composites before and after Au coating can be quite useful in biomedical applications, for separation processes and as MRI contrast agents. Since magnetic core-shell nanostructures have been shown to assemble under an applied magnetic field,⁵³ assembly of the nanoparticles into arrays or superlattices could be utilized to study plasmon coupling in long-range periodic structures, which may lead to the development of new types of photonic-magnetic nanodevices.

METHODS

Materials

Tri-n-octylamine (TOA; 98%), oleic acid (OA; 90%), tetrachloroauric acid ($\text{HAuCl}_4 \cdot 3\text{H}_2\text{O}$), Tetrakis(hydroxymethyl)phosphonium chloride (THPC, 80% solution in water), 3-Aminopropyltriethoxysilane (APTES, 98%), and hexane were purchased from Sigma-Aldrich (St. Louis, MO). Hexane was distilled using standard procedures.⁵⁴ Sodium hydroxide (NaOH, 1 N), sodium chloride (NaCl, Biological, Certified), potassium carbonate (K_2CO_3 , Certified A.C.S.) and formaldehyde (37%) were obtained from Fisher Scientific (Hampton, NH). 200 proof ethanol was obtained from Decon Laboratories, Inc. (King of

Prussia, PA). Ultrapure water (18.2 M Ω resistivity) was obtained from a Milli-Q water purification system (Millipore, Billerica, MA).

Synthesis

Reactions were carried out using standard Schlenk techniques. The formation of the iron oxide nanoparticles was accomplished by the decomposition of 0.5 g iron formate ($\text{Fe}^{\text{II}}(\text{HCOO})_2 \cdot 2\text{H}_2\text{O}$) in the presence of a tri-n-octylamine: oleic acid (7 mL:1 mL, TOA:OA) surfactant system with the addition of 100 μL of HPLC grade H_2O , under inert atmosphere at elevated temperatures (*ca.* 370 $^\circ\text{C}$). This protocol has been reported to yield nanoparticles composed of a wüstite core with magnetite-rich corners and edges.²³ The particles were then centrifuged three times for ten minutes at 2224 RCF, redispersed each time in 10 mL of dry hexane, and dried under vacuum without heating.

The precursor nanoparticle solutions used in the present study were fabricated following a similar procedure as the previously reported methods for the immobilization of Au nanoparticles on silica^{25, 26} or hematite²⁷ surfaces. The surface of the iron oxide nanoparticles was functionalized with organosilane molecules (APTES) to generate an amine terminated surface. APTES functionalization was performed by one of two methods, either by (1) centrifuging an additional three times, redispersing in 200 proof ethanol, and under vigorous stirring, the quick addition of 600 μL of APTES or by (2) silane ligand exchange, where in a glass container under ambient conditions, 0.5% (v/v) APTES was added to the nanoparticles in hexane containing 0.01% (v/v) acetic acid⁵⁵ causing precipitation of the particles. The particles were stirred overnight and then rinsed by centrifuging and redispersing with either ethanol (method 1) or water (method 2) to get rid of any excess APTES. Surface functionalization with silane ligand exchange (method 2) was used when the hydrophobic surfactant coating could not be displaced by method 1.

A colloidal gold solution yielding ~ 2 nm Au particles was prepared using THPC as the reductant according to Duff *et al.*⁵⁶ and was refrigerated for at least two weeks before use. The precursor nanoparticle solution was made by the addition of 40 mL of the aged THPC colloidal gold solution, 4 mL of 1 M NaCl, and 500 μL of APTES functionalized iron oxide nanoparticles and refrigerated overnight. The precursor solution was then centrifuged three times until the supernatant was colorless at 300 RCF for 30 minutes to remove excess free colloidal gold nanoparticles and was redispersed each time in Milli-Q water with a sonicating probe.

A 44 μM HAuCl_4 plating solution was produced by the addition 1 wt % chloroauric acid to 1.8 mM aqueous K_2CO_3 . The solution was stored for a minimum of 12 hours in the dark. Au coated iron oxide nanoparticles were synthesized by the reduction of AuCl_4^- ions in the plating solution by formaldehyde onto the precursor nanoparticles. Shell thickness was controlled by varying the ratio between the precursor particles and aqueous AuCl_4^- ions. Complete shell growth took about 10 minutes and was monitored by solution extinction measurements.

Characterization

Transmission electron microscope (TEM) micrographs were obtained using a JEOL 2010 TEM. Scanning electron microscope (SEM) images were obtained on a FEI Quanta 400 environmental SEM at an accelerating voltage of 20 kV. Extinction spectra were obtained using a Cary 5000 UV/Vis/NIR spectrophotometer. X-ray diffraction (XRD) patterns were obtained using a Rigaku Ultima II vertical θ - θ powder diffractometer (CuK α , $\lambda = 1.5418 \text{ \AA}$). XRD patterns between $20^\circ < 2\theta < 70^\circ$ were collected. Materials Data, Inc., (MDI) JADE8 software was used to subtract the background. Raman spectra were collected on a Renishaw inVia Microscope, using a 785 nm excitation source with a 1.5 mW laser power. X-ray photoemission spectroscopy (XPS) was performed on a Phi Quantera XPS spectrometer; solid samples were prepared by pressing them onto indium foil. Magnetization measurements as a function of applied field and temperature $M(H,T)$ were performed in a Quantum Design Magnetic Properties Measurement System (QD MPMS) ($T = 1.8 \text{ K} - 400 \text{ K}$, $H_{\text{max}} = 7.0 \text{ T}$).

Supplementary Material

Refer to Web version on PubMed Central for supplementary material.

Acknowledgments

The authors gratefully acknowledge Dr. Jeffrey Hartgerink, Adam Colson, Michael L. Matson, Liang Zhao, Rizia Bardhan, Janardan Kundu, Joe Cole, Nikolay Mirin, and Nathaniel K. Grady for helpful discussions. C.S. Levin was supported by a training fellowship from the Keck Center Nanobiology Training Program of the Gulf Coast Consortia, NIH 1 T90 DK070121-01. This work was also supported by the National Science Foundation (NSF) Grants EEC-0304097, EEC-0647452, and CHE-0719396, AFOSR Grant F49620-03-C-0068, the Robert A. Welch Foundation Grants C-1220, C-1222, and C-0976, and the Multidisciplinary University Research Initiative (MURI) Grant W911NF-04-01-0203.

REFERENCES

1. Insin N, Tracy JB, Lee H, Zimmer JP, Westervelt RM, Bawendi MG. Incorporation of Iron Oxide Nanoparticles and Quantum Dots into Silica Microspheres. *ACS Nano*. 2008; 2:197–202. [PubMed: 19206619]
2. Weng KC, Noble CO, Papahadjopoulos-Sternberg B, Chen FF, Drummond DC, Kirpotin DB, Wang D, Hom YK, Hann B, Park JW. Targeted Tumor Cell Internalization and Imaging of Multifunctional Quantum Dot-Conjugated Immunoliposomes in Vitro and in Vivo. *Nano Lett*. 2008; 8:2851–2857. [PubMed: 18712930]
3. Halas NJ. Playing with Plasmons: Tuning the Optical Resonant Properties of Nanoshells. *MRS Bulletin*. 2005; 30:362–367.
4. Wang H, Brandl D, Nordlander P, Halas NJ. Plasmonic Nanoparticles: Artificial Molecules. *Acc. Chem. Res*. 2007; 40:53–62.
5. Prodan E, Nordlander P, Halas NJ. Effects of Dielectric Screening on the Optical Properties of Metallic Nanoshells. *Chem. Phys. Lett*. 2003; 368:94–101.
6. Chiang I-C, Chen D-H. Synthesis of Monodisperse FeAu Nanoparticles with Tunable Magnetic and Optical Properties. *Adv. Funct. Mater*. 2007; 17:1311–1316.
7. Carpenter EE, Kumbhar A, Wiemann JA, Srikanth H, Wiggins J, Zhou WL, O'Connor CJ. Synthesis and Magnetic Properties of Gold-Iron-Gold Nanocomposites. *Mater. Sci. Eng., A*. 2000; 286:81–86.
8. Chen M, Yamamuro S, Farrell D, Majetich SA. Gold-Coated Iron Nanoparticles for Biomedical Applications. *J. Appl. Phys*. 2003; 93:7551–7553.

9. Cho S-J, Jarrett BR, Louie AY, Kauzlarich SM. Gold-Coated Iron Nanoparticles: A Novel Magnetic Resonance Agent for T1 and T2 Weighted Imaging. *Nanotechnology*. 2006; 17:640–44.
10. Lim J, Tilton RD, Eggeman A, Majetich SA. Design and Synthesis of Plasmonic Magnetic Nanoparticles. *J. Magn. Magn. Mater.* 2007; 311:78–83.
11. Mikhaylova M, Kim DK, Bobrysheva N, Osmolowsky M, Semenov V, Tsakalatos T, Muhammed M. Superparamagnetism of Magnetite Nanoparticles: Dependence on Surface Modification. *Langmuir*. 2004; 20:2472–2477. [PubMed: 15835712]
12. Shevchenko EV, Bodnarchuk MI, Kovalenko MV, Talapin DV, Smith RK, Aloni S, Heiss W, Alivisatos AP. Gold/Iron Oxide Core/Hollow-Shell Nanoparticles. *Adv. Mater.* 2008; 20:4323–4329.
13. Stoeva SI, Huo F, Lee J-S, Mirkin CA. Three-Layer Composite Magnetic Nanoparticle Probes for DNA. *J. Am. Chem. Soc.* 2005; 127:15362–15363. [PubMed: 16262387]
14. Salgueiriño-Maceira V, Correa-Duarte MA, Farle M, López-Quintela A, Sieradzki K, Diaz R. Bifunctional Gold-Coated Magnetic Silica Spheres. *Chem. Mater.* 2006; 18:2701–2706.
15. Schotter J, Bethge O, Maier T, Brueckl H. Recognition of Biomolecular Interactions by Plasmon Resonance Shifts in Single- and Multicomponent Magnetic Nanoparticles. *Appl. Phys. Lett.* 2008; 93:144105.
16. Yin M, O'Brien S. Synthesis of Monodisperse Nanocrystals of Manganese Oxides. *J. Am. Chem. Soc.* 2003; 125:10180–10181. [PubMed: 12926934]
17. Redl FX, Black CT, Papaefthymiou GC, Sandstrom RL, Yin M, Zeng H, Murray CB, O'Brien S. Magnetic, Electronic, and Structural Characterization of Nonstoichiometric Iron Oxides at the Nanoscale. *J. Am. Chem. Soc.* 2004; 126:14583–14599. [PubMed: 15521779]
18. Yin M, Chen Z, Deegan B, O'Brien S. Wüstite Nanocrystals: Synthesis, Structure, and Superlattice Formation. *J. Mater. Res.* 2007; 22:1987–1989.
19. Park J, An K, Hwang Y, Park J-G, Noh H-J, Kim J-Y, Park J-H, Hwang N-M, Hyeon T. Ultra-Large-Scale Syntheses of Monodisperse Nanocrystals. *Nat. Mater.* 2004; 3:891–895. [PubMed: 15568032]
20. Palnichenko AV, Rossolenko AN, Kopylov VN, Zver'kova II, Aronin AS. Synthesis of Wustite Nanowires by Carbon Plasma Pulse Assisted Method. *Chem. Phys. Lett.* 2005; 410:436–440.
21. Emel'yanov DA, Korolev KG, Mikhailenko MA, Knot'ko AV, Oleinikov NN, Tret'yakov YD, Boldyrev VV. Mechanochemical Synthesis of Wüstite, Fe_{1-x}O , in High-Energy Apparatuses. *Inorg. Mater.* 2004; 40:632–635.
22. Matteazzi P, Le Caër G. Reduction of Haematite with Carbon by Room Temperature Ball Milling. *Mater. Sci. Eng., A*. 1991; 149:135–142.
23. Hofmann C, Rusakova I, Ould-Ely T, Prieto-Centurión D, Hartman KB, Kelly AT, Lüttge A, Whitmire KH. Shape Control of New $\text{Fe}_x\text{O-Fe}_3\text{O}_4$ and $\text{Fe}_{1-y}\text{Mn}_y\text{O-Fe}_{3-z}\text{Mn}_z\text{O}_4$ Nanostructures. *Adv. Funct. Mater.* 2008; 18:1661–1667.
24. Gould P. Nanoparticles Probe Biosystems. *Mater. Today*. 2004; 7:36–43.
25. Oldenburg SJ, Averitt RD, Westcott SL, Halas NJ. Nanoengineering of Optical Resonances. *Chem. Phys. Lett.* 1998; 288:243–247.
26. Brinson BE, Lassiter JB, Levin CS, Bardhan R, Mirin N, Halas NJ. Nanoshells Made Easy: Improving Au Layer Growth on Nanoparticle Surfaces. *Langmuir*. 2008; 24:14166–14171. [PubMed: 19360963]
27. Wang H, Brandl DW, Le F, Nordlander P, Halas NJ. Nanorice: A Hybrid Plasmonic Nanostructure. *Nano Lett.* 2006; 6:827–832. [PubMed: 16608292]
28. Oldenburg SJ, Jackson JB, Westcott SL, Halas NJ. Infrared Extinction Properties of Gold Nanoshells. *Appl. Phys. Lett.* 1999; 75:2897–2899.
29. Xu Z, Hou Y, Sun S. Magnetic Core/Shell $\text{Fe}_3\text{O}_4/\text{Au}$ and $\text{Fe}_3\text{O}_4/\text{Au}/\text{Ag}$ Nanoparticles with Tunable Plasmonic Properties. *J. Am. Chem. Soc.* 2007; 129:8698–8699. [PubMed: 17590000]
30. Taton TA, Lu G, Mirkin CA. Two-Color Labeling of Oligonucleotide Arrays via Size- Selective Scattering of Nanoparticle Probes. *J. Am. Chem. Soc.* 2001; 123:5164–5165. [PubMed: 11457374]

31. Cao YC, Jin R, Mirkin CA. DNA-Modified Core-Shell Ag/Au Nanoparticles. *J. Am. Chem. Soc.* 2001; 123:7961–7962. [PubMed: 11493092]
32. Prodan E, Radloff C, Halas NJ, Nordlander P. A Hybridization Model for the Plasmon Response of Complex Nanostructures. *Science.* 2003; 302:419–422. [PubMed: 14564001]
33. Prodan E, Nordlander P. Plasmon Hybridization in Spherical Nanoparticles. *J. Chem. Phys.* 2004; 120:5444–5454. [PubMed: 15267418]
34. Johnson PB, Christy RW. Optical Constants of the Noble Metals. *Phys. Rev. B.* 1972; 6:4370–4379.
35. Hao F, Nordlander P. Efficient Dielectric Function for FDTD Simulation of the Optical Properties of Silver and Gold Nanoparticles. *Chem. Phys. Lett.* 2007; 446:115–118.
36. Wang H, Wu Y, Lassiter B, Nehl CL, Hafner JH, Nordlander P, Halas NJ. Symmetry-Breaking in Individual Plasmonic Nanoparticles. *Proc. Nat. Acad. Sci. U.S.A.* 2006; 103:10856–10860.
37. Wu YP, Nordlander P. Plasmon Hybridization in Nanoshells with a Nonconcentric Core. *J. Chem. Phys.* 2006; 125:124708. [PubMed: 17014201]
38. Querry, MR. Optical Constants. University of Missouri; 1985.
39. Henning T, Begemann B, Mutschke H, Dorschner J. Optical Properties of Oxide Dust Grains. *Astron. Astrophys. Suppl. Ser.* 1995; 112:143–149.
40. Gole A, Stone JW, Gemmill WR, zur Loye H-C, Murphy CJ. Iron Oxide Coated Gold Nanorods: Synthesis, Characterization, and Magnetic Manipulation. *Langmuir.* 2008; 24:6232–6237. [PubMed: 18484755]
41. de Faria DLA, Silva SV, de Oliveira MT. Raman Microspectroscopy of Some Iron Oxides and Oxyhydroxides. *J. Raman Spec.* 1997; 28:873–878.
42. Shechter H, Hillman P, Ron M. Mössbauer Study of the Structure and Decomposition of Wüstite. *J. Appl. Phys.* 1966; 37:3043–3047.
43. Cullity, BD.; Stock, SR. Elements of X-ray Diffraction. Prentice Hall; Upper Saddle River, NJ: 2001.
44. Shull CG, Strausser WA, Wollan EO. Neutron Diffraction by Paramagnetic and Antiferromagnetic Substances. *Phys. Rev.* 1951; 83:333–345.
45. Bizette H, Tsai B. Colloque Sur La Polarization De La Matière. *C. R. Acad. Sci., Paris.* 1943; 217:390.
46. Stöhr, J.; Siegmann, HC. Magnetism. Springer; New York:
47. Kittel, C. Introduction to Solid State Physics. John Wiley & Sons, Inc.; Hoboken, NJ: 2005.
48. Fjellvåg H, Hauback BC, Vogt T, Stølen S. Monoclinic Nearly Stoichiometric Wüstite at Low Temperatures. *Am. Mineral.* 2002; 87:347–349.
49. Morrish, AH. The Physical Principles of Magnetism. John Wiley & Sons, Inc.; 1965.
50. Crespo P, Litrán R, Rojas TC, Multigner M, de la Fuente JM, Sánchez-López JC, Garcá MA, Hernando A, Penadés S, Fernández A. Permanent Magnetism, Magnetic Anisotropy, and Hysteresis of Thiol-Capped Gold Nanoparticles. *Phys. Rev. Lett.* 2004; 93:087204–1-4. [PubMed: 15447222]
51. Hori H, Yamamoto Y, Iwamoto T, Miura T, Teranishi T, Miyake M. Diameter Dependence of Ferromagnetic Spin Moment in Au Nanocrystals. *Phys. Rev. B.* 2004; 69:174411–1-5.
52. Reich S, Leitus G, Feldman Y. Observation of Magnetism in Au Thin Films. *Appl. Phys. Lett.* 2006; 88:222502–1-3.
53. Zhou WL, Carpenter EE, Lin J, Kumbhar A, Sims J, O'Connor CJ. Nanostructures of Gold Coated Iron Core-Shell Nanoparticles and the Nanobands Assembled Under Magnetic Field. *Eur. Phys. J. D.* 2001; 16:289–292.
54. Perrin, DD.; Armarego, WL. Purification of Laboratory Chemicals. 5th ed.. Pergamon Press; New York: 1993.
55. De Palma R, Peeters S, Van Bael MJ, Van den Rul H, Bonroy K, Laureyn W, Mullens J, Borghs G, Maes G. Silane Ligand Exchange to Make Hydrophobic Superparamagnetic Nanoparticles Water-Dispersible. *Chem. Mater.* 2007; 19:1821–1831.
56. Duff DG, Baiker A, Edwards PP. A New Hydrosol of Gold Clusters. 1. Formation and Particle Size Variation. *Langmuir.* 1993; 9:2301–2309.

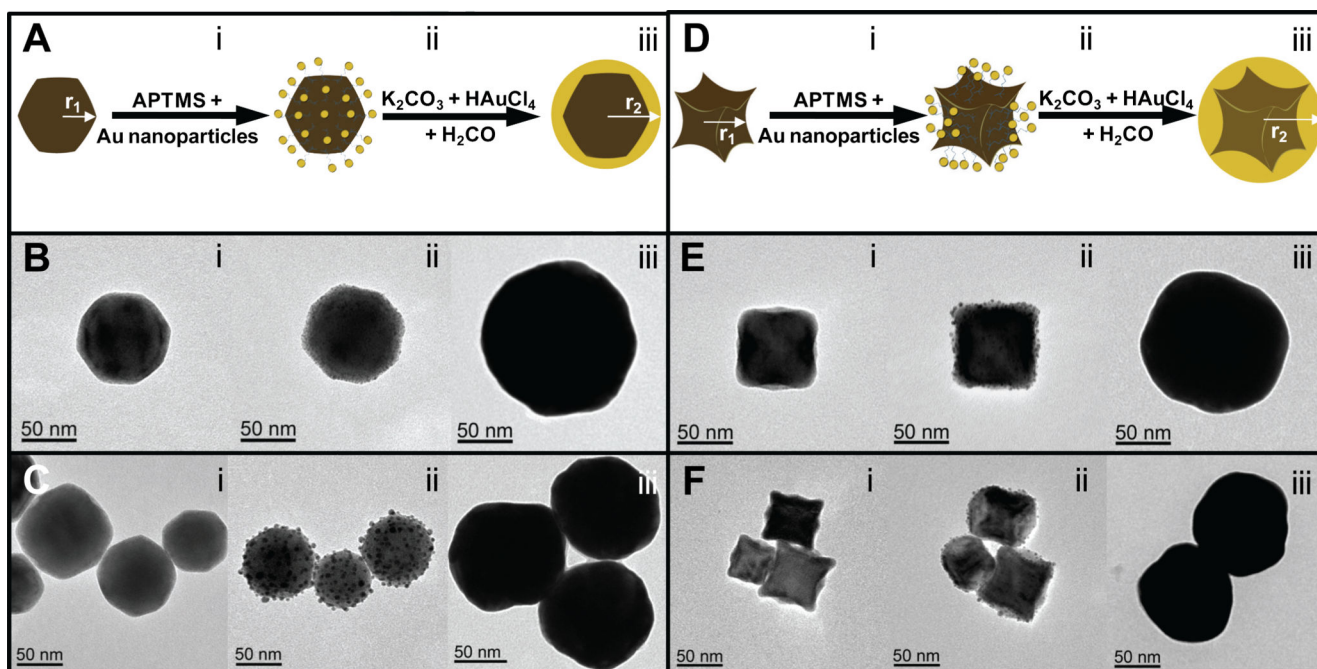


Figure 1. Schematic of Au coated iron oxide synthesis for (A) faceted and (D) tetracubic (i) core, (ii) Au decorated precursor, and (iii) Au coated iron oxide nanoparticles. TEM images representing various stages of synthesis for (B, C) faceted and (E, F) tetracubic (i) core (with average $r_1 = 31.5 \pm 9.7$ nm and 28.5 ± 7.3 nm), (ii) Au nanoparticle decorated precursor, and (iii) Au coated iron oxide nanoparticles.

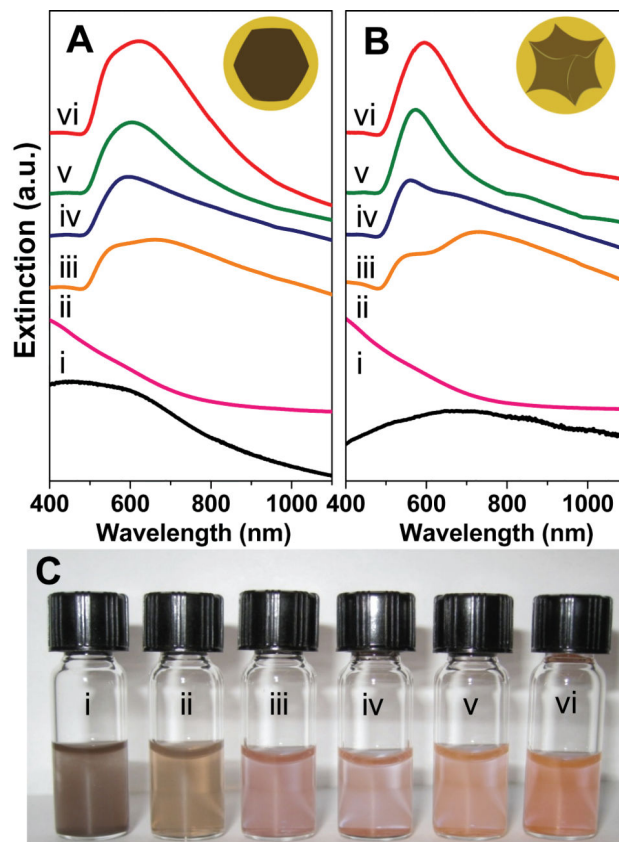


Figure 2. Solution extinction measurements of (A) faceted (B) and tetracubic gold coated iron oxide (i) ethanolic uncoated cores ($r_1 = 31.5 \pm 9.7$ and 28.5 ± 7.3 nm), (ii) Au-decorated precursor nanoparticles ($r_1 = 32.6 \pm 9.0$ and 28.6 ± 8.5 nm) in aqueous solution, and (iii-vi) Au coated nanoparticles with increasing Au thicknesses (number of particles sized is 100, r_2 is 59.9 ± 12.4 , 65.0 ± 19.9 , 73.1 ± 11.7 , and 76.6 ± 9.8 nm for the faceted cores and 40.0 ± 6.7 , 49.1 ± 10.7 , 53.8 ± 4.6 , and 66.4 ± 5.0 nm for the tetracubic cores in aqueous solution. (Spectra offset for clarity.) (C) Optical image of particles shown in A.

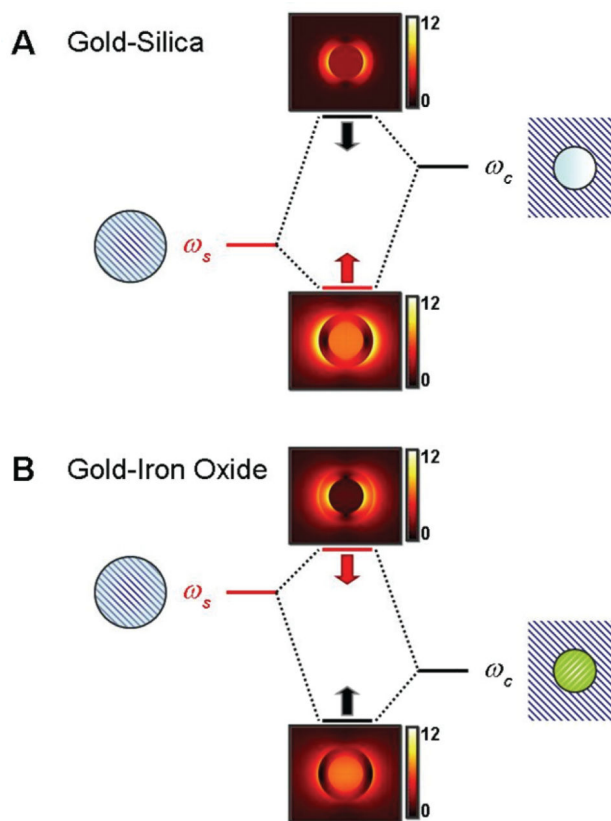


Figure 3. Hybridization in a nanoshell (A) with a low permittivity core, *e.g.*, silica, and (B) with a high permittivity core, *e.g.*, iron oxide. Dark (black) and bright (red) plasmon modes are shown in each case. Arrows show the shift of the hybridized plasmon modes with increasing shell layer thickness. The colored insets show local electric field enhancements for the spherical-core geometries in Figure 4A,B. A silica core is selected for insets in (A) showing dark (A-upper) and bright (A-lower) modes. A high permittivity core ($\epsilon = 12.0$) is selected for insets in (B) showing bright (B-upper) and dark (B-lower) modes. The inner radius of the core is $r_1 = 32$ nm and the outer radius of the shell is $r_2 = 50$ nm. A Drude model is used to represent the shell layer dielectric properties.

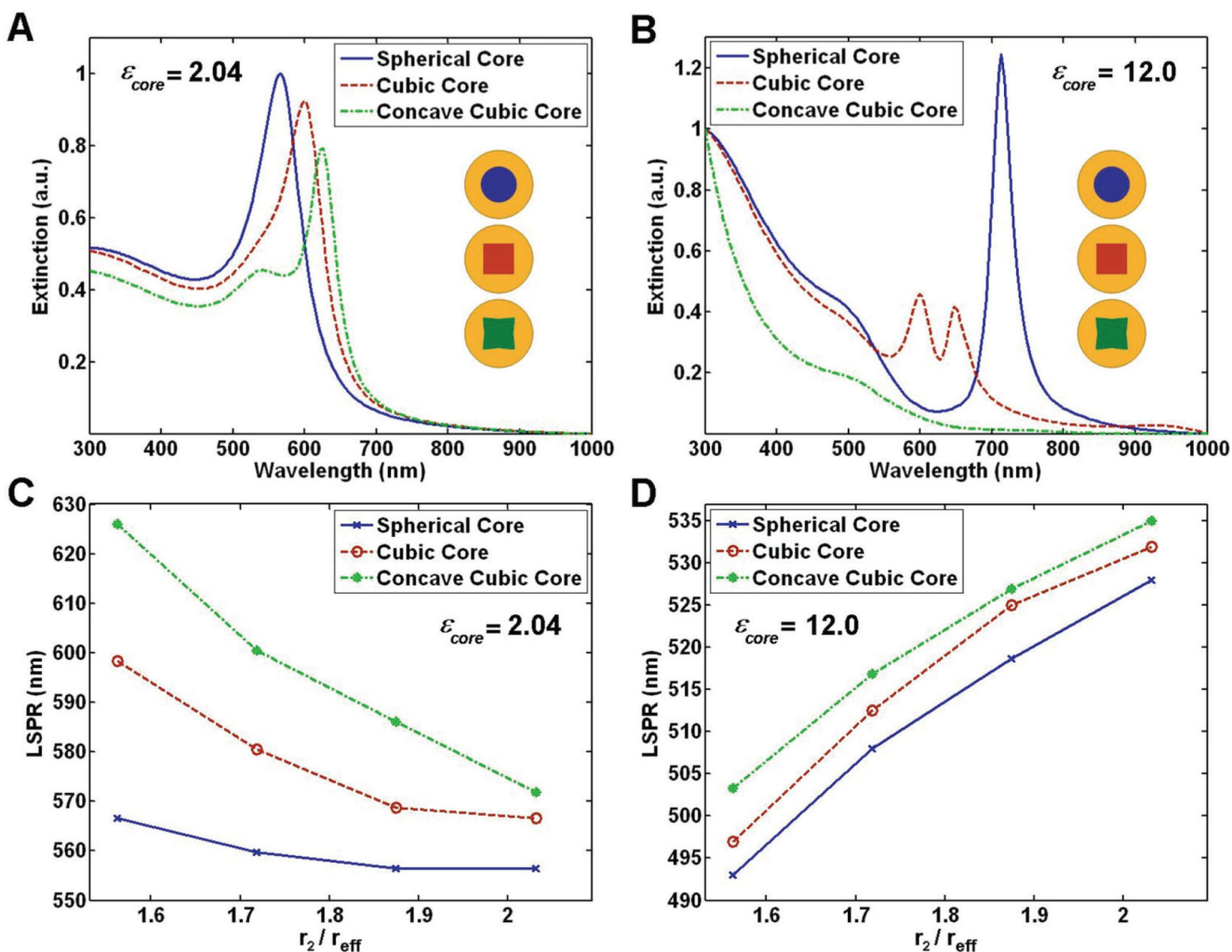


Figure 4.

(A,B) Theoretical comparison of extinction spectra for nanoshells with cores of different shapes: spherical (blue solid line), cubic (red dashed line), and concave cubic (green dash-dotted line). The outer radius of the shell is $r_2 = 50$ nm and the effective radius of the core is $r_{eff} = 32$ nm. The core dielectrics are (A) silica ($\epsilon = 2.04$) and (B) an artificial material with $\epsilon = 12.0$. (C,D) Calculated LSPR shifts of the (C) bonding dipolar nanoshell resonances for a silica core and (D) antibonding dipolar nanoshell resonances for an artificial core with $\epsilon = 12.0$, as a function of the ratio of the outer radius of the shell, r_2 , to the effective core radius $r_{eff} = 32$ nm.

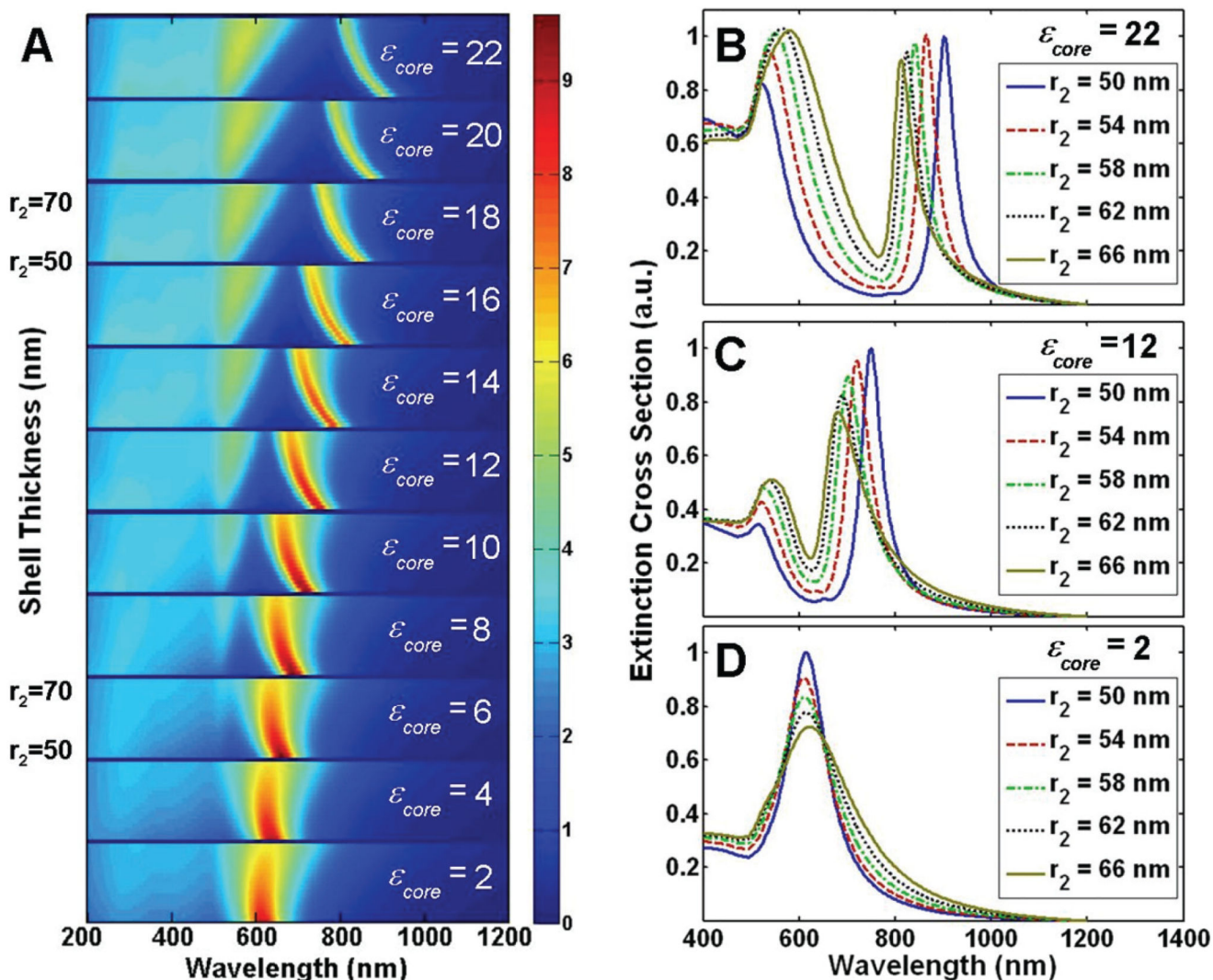


Figure 5.

(A) Theoretical color contour representation of the extinction spectra for different core dielectric permittivities and shell thicknesses for the same effective core radius of $r_{eff} = r_1 = 36$ nm. Each panel shows the extinction spectra for a fixed ϵ_{core} with the shell radius increasing from $r_2 = 50$ to $r_2 = 70$ nm. The color corresponds to the extinction cross-section values normalized to the maximum extinction value. The surrounding medium is water (dielectric constant of 1.77). (B-D) Theoretically calculated extinction spectra for spherical nanoshells with different shell thicknesses (where $r_{eff} = r_1 = 36$ nm) normalized to the thinnest shell extinction peak, using a (B) high core dielectric permittivity of 22, (C) core dielectric permittivity of 12, and (D) low core dielectric permittivity of 2. The bright mode does not significantly shift in (D) and redshifts in (B) to higher wavelengths. The best match to the experimental data is shown in (C).

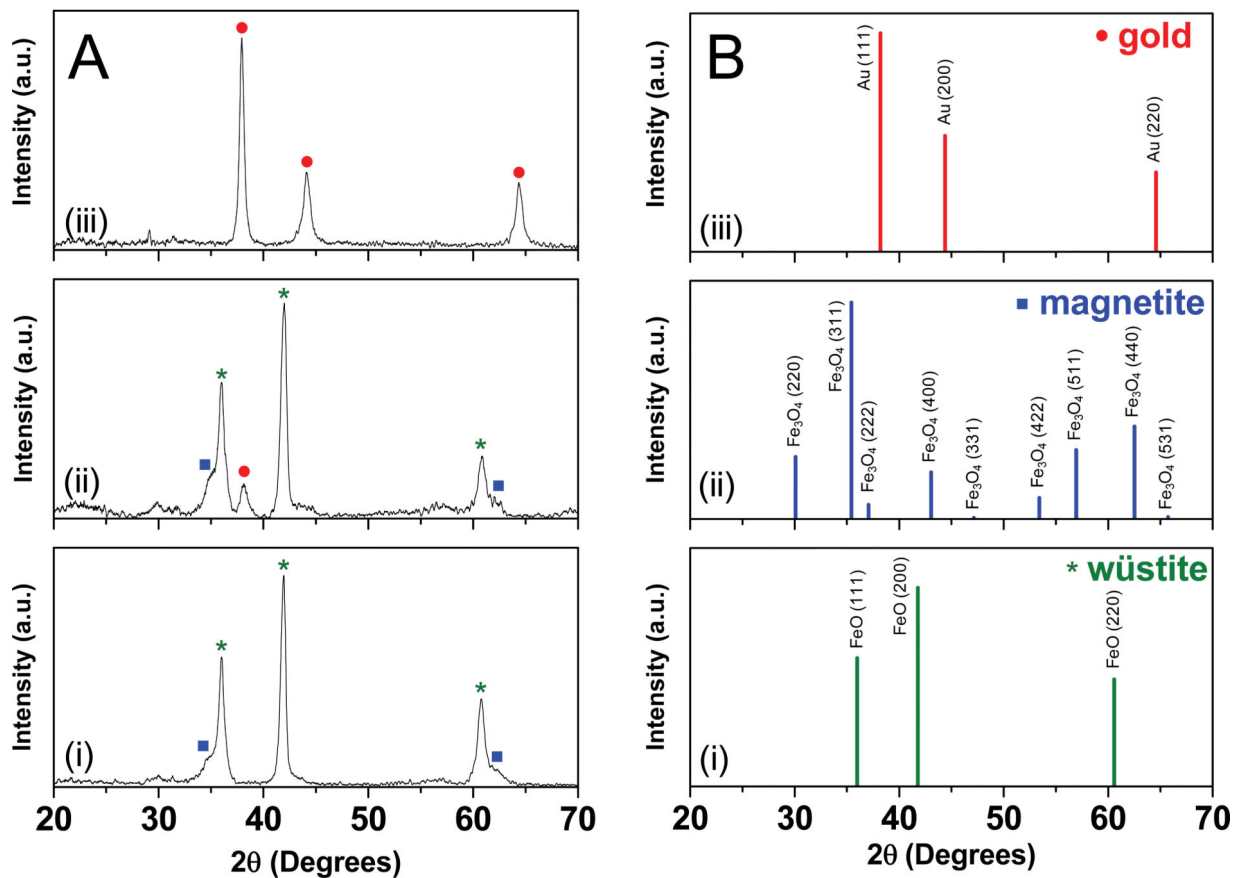


Figure 6. Powder X-ray diffraction patterns for (i) iron oxide core nanoparticles (tetracubes), (ii) Au nanoparticle decorated precursors, and (iii) Au coated iron oxide nanoparticles (with 10.9 nm shell thickness). (B) XRD peak positions for (i) wüstite, (ii) magnetite, and (iii) gold.

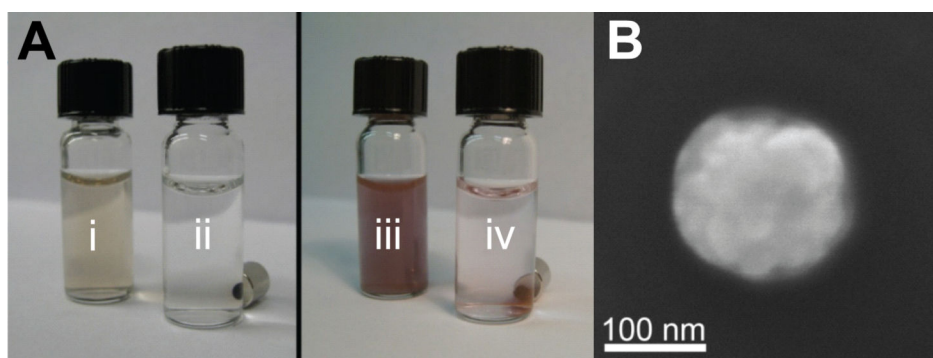


Figure 7. (A) Optical images of (i) Au-decorated iron oxide precursor particles, (ii) Au-decorated iron oxide precursor particles with magnet, (iii) Au coated nanoparticles, and (iv) Au coated nanoparticles with magnet. (B) Representative SEM image of the shells shown in (iv).

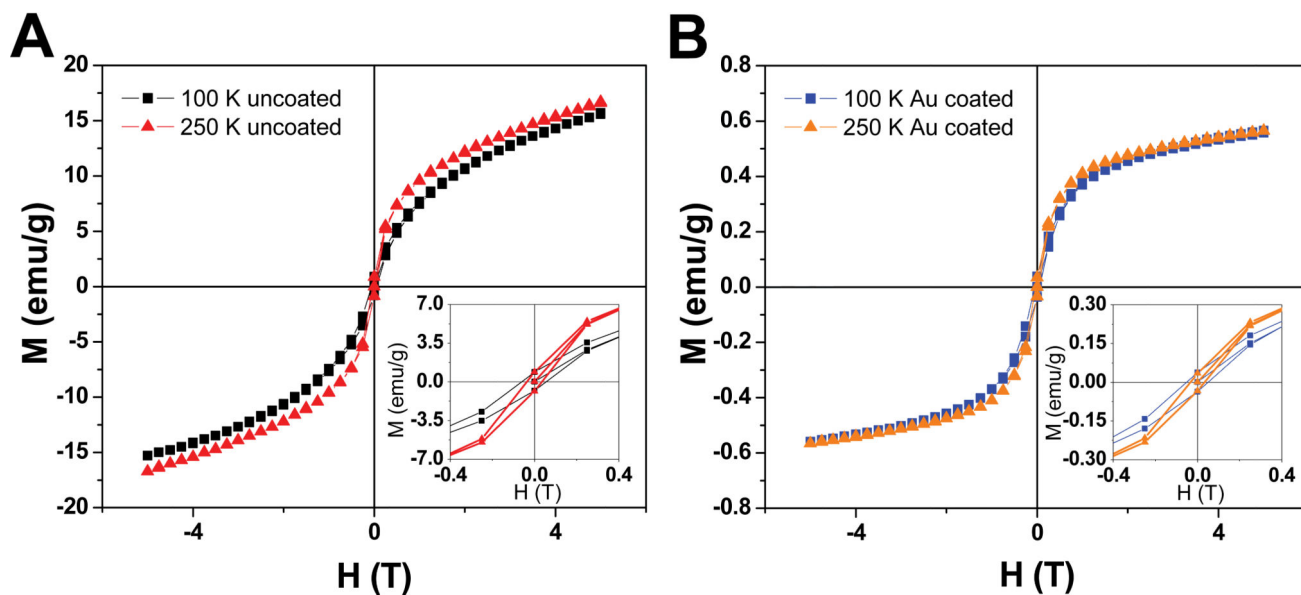


Figure 8. Magnetization as a function of magnetic field at constant temperature (100 K or 250 K) for (A) uncoated and (B) Au coated iron oxide nanoparticles (tetracubic, with 10.9 nm shell thickness, where insets show the magnetic hysteresis).